Carbon Trends 3 (2021) 100036

Contents lists available at ScienceDirect

Carbon Trends

journal homepage: www.elsevier.com/locate/cartre

First-principles investigation of electronic, optical, mechanical and heat transport properties of pentadiamond: A comparison with diamond

Bohayra Mortazavi[a], Fazel Shojaei[b], Xiaoying Zhuang[a], Luiz Felipe C. Pereira[c,*]

[a] Chair of Computational Science and Simulation Technology, Institute of Photonics, Department of Mathematics and Physics, Leibniz Universität Hannover, Appelstraße 11, 30167 Hannover, Germany
[b] Department of Chemistry, Faculty of Sciences, Persian Gulf University, Boushehr 75168, Iran
[c] Departamento de Física, Universidade Federal de Pernambuco, Recife, 50670-901, Brazil

ARTICLE INFO

Article history:
Received 17 December 2020
Revised 5 February 2021
Accepted 5 February 2021

ABSTRACT

Pentadiamond is a carbon allotrope consisting of hybrid sp^2 and sp^3 atoms, which has been predicted to be stable and synthesizable. In this work we employ first-principles calculations to explore the electronic structure, optical characteristics, mechanical response and lattice thermal conductivity of pentadiamond, performing a direct comparison with the corresponding properties in diamond. The HSE06 density functional predicts indirect electronic band gaps for pentadiamond and diamond with values of 3.58 eV and 5.27 eV, respectively. Results for optical characteristics reveal pentadiamond's large absorption in the middle UV region, where diamond does not absorb light, consistent with the smaller band gap of pentadiamond. The elastic modulus and tensile strength of pentadiamond are found to be 496 GPa and 60 GPa, respectively, considerably lower than the corresponding values for diamond. The lattice thermal conductivity is examined by solving the Boltzmann transport equation, with anharmonic force constants evaluated via state-of-the-art machine-learning interatomic potentials. We predict a thermal conductivity of 427 W/m-K for pentadiamond, less than one fifth of the corresponding quantity for diamond. Our results provide a useful vision of the intrinsic properties of pentadiamond, but also highlight some of its disadvantages in mechanical strength and heat conduction when compared to diamond.

1. Introduction

The chemical versatility of carbon atoms allows them to exist with sp, sp^2 and sp^3 orbital hybridizations, which reflect in diverse all-carbon structures. In bulk, diamond is the most stable carbon allotrope with its complete sp^3 hybridized atoms. In lower dimensions, carbon atoms form fullerenes [1], carbon nanotubes [2] and graphene [3–5], all of which contain exclusively sp^2 hybridized atoms. Carbon nanotubes and graphene exhibit ultrahigh mechanical strength and thermal conductivity, in most part due to the carbon sp^2 bonds [6–10]. In spite of the superior stability of graphene, it is also possible to produce two-dimensional carbon structures which are not limited to a full sp^2 lattice. In fact, more than three decades ago, Baughman et al. [11] predicted numerous forms of hybrid sp and sp^2 carbon nanoporous 2D lattices, so called graphdiynes. Indeed, since 2010, different full-carbon graphdiyne structures have been experimentally realized [12,13].

The presence of sp, sp^2 or sp^3 hybridizations in 2D carbon allotropes can be used to open an electronic band gap, improve their stretchability or modify their thermal properties [14–20]. Therefore, modification of hybridization states appears to be an effective approach to tailor electronic, mechanical, optical and thermal properties of carbon allotropes. In a very recent theoretical work Fujii and coworkers [21] predicted a metastable three-dimensional carbon allotrope with mixed sp^2 and sp^3 hybridization, which they named *pentadiamond*. Unlike pristine diamond, in which every carbon atom bonds with four neighboring atoms, in pentadiamond a carbon atom bonds with either three or four neighboring carbons, as illustrated in Fig. 1.

In their work, Fujii et al. proposed that pentadiamond could be produced via copolymerization of hydrocarbon molecules containing pentagonal rings. Their total energy calculations showed that the structure was stable and presented a semiconductor character with a band gap about half of the value for diamond. They

* Corresponding author.
E-mail addresses: bohayra.mortazavi@gmail.com (B. Mortazavi), pereira@df.ufpe.br (L.F.C. Pereira).

https://doi.org/10.1016/j.cartre.2021.100036

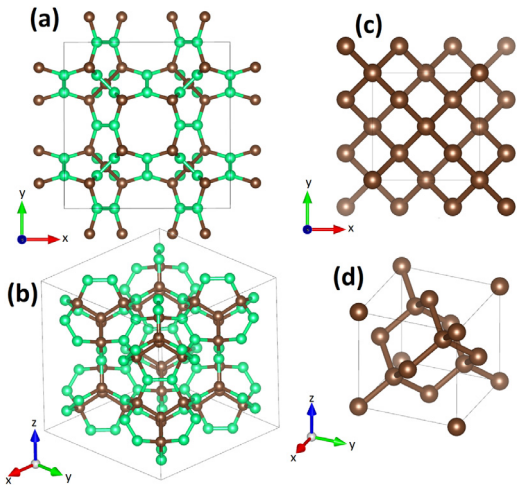

Fig. 1. Crystal structure of pentadiamond (a, b) and diamond (c, d). The conventional cubic cell contains 22 carbon atoms for pentadiamond and 8 atoms for diamond. In (a) and (b) the lighter color indicates sp^2 hybridized atoms.

also found that pentadiamond presented remarkable mechanical properties: a relatively high bulk modulus (approximately 80% of the corresponding value for diamond) along with a negative Poisson ratio. Pentadiamond was also predicted to possess very high Young's and shear moduli, surpassing those of diamond. Unfortunately, soon after publication, independent research groups were unable to reproduce some of the results concerning pentadiamond's remarkable mechanical properties, particularly its negative Poisson ratio, and the manuscript has since been retracted [22]. Nonetheless, no concerns were raised in relation to the possible synthetic route and thermodynamic stability of pentadiamond.

In the present study we aim to investigate the structural stability as well as electronic, mechanical, and optical properties of pentadiamond via extensive density functional theory (DFT) calculations. In order to provide a broader vision, those properties were directly compared to the predicted properties of pristine diamond. We also employ state-of-the-art machine-learning interatomic potentials to estimate and compare the thermal conductivity of pentadiamond and diamond. Our results reveal that by altering the full sp^3 hybridization in pristine diamond to a mixture of sp^2 and sp^3 hybridizations in pentadiamond, the mechanical properties and thermal conductivity are substantially suppressed. However, we confirm that this novel bulk carbon allotrope is indeed a semiconductor, and predict high absorption of visible light due to the smaller electronic band gap when compared to diamond.

2. Methods

Density functional theory calculations in this work were performed in the Vienna Ab-initio Simulation Package (VASP) [23–25], implementing the Perdew-Burke-Ernzerhof generalized gradient approximation (GGA/PBEsol) functional, which provides improved equilibrium properties for densely-packed solids [26,27]. All calculations were carried out with an energy cutoff of 500 eV for the plane waves. Energy minimization was achieved with the conjugate gradient approach with convergence criteria of 10^{-4} eV and 0.005 eV/Å for energy and forces, respectively, employing a 9×9×9 Monkhorst-Pack k-point grid [28]. Electronic and optical features were calculated with a convergence criterion of 10^{-6} eV for the electronic self-consistent-loop. Since GGA/PBESol underestimates the position of conduction band maxima and systematically underestimate the band gap, the screened hybrid functional of HSE06 [29,30] was employed to provide more accurate estimations for the electronic and optical properties. HSE06 calculations employed 8×8×1 and 18×18×1 k-point meshes for pentadiamond and diamond, respectively.

We examined the light absorption properties of both materials by calculating their frequency-dependent complex dielectric function $\epsilon = \epsilon_1 + \imath\epsilon_2$, neglecting local field effects. The imaginary part is given by direct interband transitions through Fermi's golden rule,

$$\epsilon_2(\omega) = \frac{4\pi^2}{\Omega\omega^2} \sum_{i\in \mathrm{VB},\ j\in \mathrm{CB}} \sum_k W_k \left|\rho_{ij}\right|^2 \delta(\varepsilon_{kj} - \varepsilon_{ki} - \hbar\omega), \tag{1}$$

where VB and CB denote the valence and conduction bands, ω is the photon frequency, Ω is the unit cell volume, and ρ_{ij} is the dipole transition matrix element. W_k is the weight of the respective k-point in the reciprocal space. For the real part, we recall that ϵ_1 and ϵ_2 are related through the Kramers-Kronig relation [31]

$$\epsilon_1(\omega) = 1 + \frac{1}{\pi} P \int_0^\infty d\omega' \frac{\omega'\epsilon_2(\omega')}{\omega'^2 - \omega^2}, \tag{2}$$

where P denotes the principal value. Finally, the absorption coefficient α, can be calculated as

$$\alpha(\omega) = \sqrt{2}\omega\left[\sqrt{\epsilon_1^2(\omega) + \epsilon_2^2(\omega)} - \epsilon_1(\omega)\right]^{1/2}. \tag{3}$$

The mechanical response was probed by conducting uniaxial tensile deformations on rectangular unit cells including 88 and 8 atoms, with 3×3×3 and 9×9×9 k-point grids, respectively, for pentadiamond and diamond. The stress-free geometry-optimized hexagonal and rectangular unit cells in the VASP POSCAR format are included in the Supplementary Information. Density functional perturbation theory (DFPT) calculations with 2×2×2 and 5×5×5 supercells were carried out to acquire the harmonic force constants for pentadiamond and diamond, respectively. From the DFPT inputs, phonon dispersion relations were computed with PHONOPY [32].

Finally, we have also developed state-of-the-art machine-learning interatomic potentials to evaluate phonon group velocities and lattice thermal conductivities. To this aim we trained moment tensor potentials (MTPs) [33], which are accurate and computationally efficient models to describe the interatomic forces [34–36]. The training sets were prepared by conducting ab-initio molecular dynamics (AIMD) simulations at 50, 300 and 800 K, each for 1000 time steps over rectangular supercells including 176 and 144 carbon atoms for pentadiamond and diamond, respectively, employing a 2×2×2 k-point grid. MTPs with 901 parameters were then passively fitted using the procedure described in our recent studies [37,38]. Once again, PHONOPY was employed to obtain phonon dispersion relations using the trained MTPs for the interatomic force calculations, and compared to the DFPT dispersions.

Anharmonic interatomic force constants were calculated using the trained MTPs over 2×2×2 and 5×5×5 supercells for pentadiamond and diamond, respectively, taking into account the interactions up to fourth nearest neighbors. In total, anharmonic force constants required 572 calculations with 176 atoms for pentadiamond and 80 calculations with 250 atoms for pentadiamond. The computational cost to perform those calculations fully ab-initio, i.e. without the MTPs, would be essentially prohibitive for most research groups worldwide. Lattice thermal conductivities were calculated from a full iterative solution of the Boltzmann transport equation using the ShengBTE package [39], with harmonic and anharmonic interatomic force constants from DFPT and MTP. In order to estimate the thermal conductivity of naturally occurring structures, isotope scattering is considered in the Boltzmann transport solution. Complete computational details for the MTP/ShengBTE coupling can be found in [38].

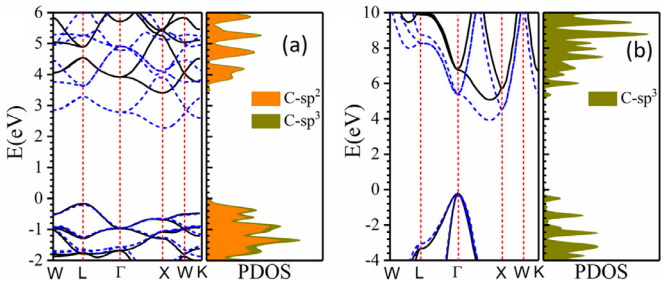

Fig. 2. Electronic band structure and projected density of states of (a) pentadiamond and (b) diamond crystal structures calculated using PBE (dashed blue lines) and HSE06 (solid black lines) functionals.

3. Results and Discussion

We begin by calculating the lattice constants for diamond and pentadiamond, both of which present cubic symmetry. In the case of diamond we obtain a lattice constant of 3.557 Å, which is an excellent agreement with the experimentally measured value of 3.567 Å. Meanwhile, for pentadiamond we obtain a lattice constant equal to 9.153 Å, consistent with the larger size of its unit cell in comparison to diamond, and in good agreement with recent studies [40,41].

We then move on to the calculation of the electronic structure for both carbon allotropes. Electronic band structures and projected density of states (PDOS) calculated with the HSE06 functional are shown in Fig. 2. From these results it is apparent that pentadiamond is a wide-band gap semiconductor with an energy gap of 3.58 eV. For comparison, we find a PBESol band gap of 2.48 eV, in a very good agreement with the value of 2.52 eV reported by Fujii et al in the original (now retracted) pentadiamond work [21,22]. In the case of diamond, HSE06 yields a 5.27 eV band gap, also remarkably close to the experimentally reported value of 5.5 eV [42]. Both allotropes present an indirect band gap, and for pentadiamond the valence band maximum (VBM) is located at the *L* point while the conduction band minimum (CBM) is at the *X* point of the first Brillouin zone.

Comparing the electronic structure of pentadiamond and diamond, two major differences can be observed at first glance. First, the computed band gap of pentadiamond (3.58 eV) is smaller than that of diamond (5.27 eV), but still within the semiconductor range. Second, in diamond both valence and conduction bands show sharper peaks, indicating higher electron and hole mobilities. Indeed, diamond has been shown to have the highest electron and hole mobilities at room temperature among wide-band gap semiconductors [43].

In order to rationalize the observed differences, we compute the partial charge density distribution at VBM and CBM for both allotropes, as shown in Fig. 3. In the case of pentadiamond both VBM and CBM are almost exclusively formed by contributions from isolated sp^2 carbon pairs in a way that VBM represents a bonding π(C-C) state, while CBM is an antibonding π^*(C-C) state. Our PDOS analysis (shown in Fig. 2) reveals that electronic states in the energy range from -2 eV to 6 eV are also mainly due to isolated sp^2 carbon pairs with bonding (below the Fermi level) and antibonding (above the Fermi level) π character. For diamond, however, both VBM and CBM are fully delocalized states, extending over the entire crystal lattice in a way that VBM represents a bonding σ(C-C) state, while CBM is an antibonding σ^*(C-C) state.

From the general chemistry of carbon we know that π(C-C) bonds are weaker than σ(C-C) bonds and they appear at higher energies, while the corresponding antibonding π^*(C-C) states lie at lower energies compared to the antibonding σ^*(C-C). This results in a smaller band gap for pentadiamond, when compared

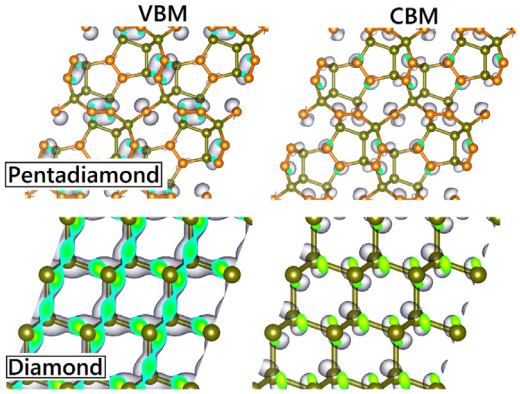

Fig. 3. Charge density distribution of VBM and CBM states of pentadiamond and diamond. In the upper diagrams, orange and green spheres indicate carbon atoms with sp^2 and sp^3 orbital hybridizations, respectively. The isosurface values are 0.01 and 0.06 e/Å^3 for pentadiamond and diamond, respectively.

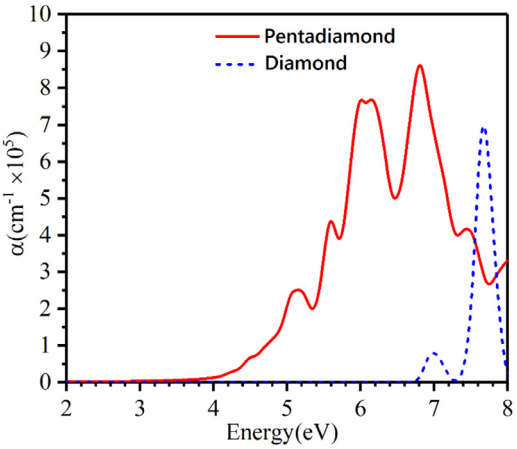

Fig. 4. Absorption coefficients of pentadiamond and diamond calculated using HSE06 functional. Pentadiamond shows large absorption in the middle UV range.

to diamond. In addition, since both valence and conduction bands present contributions from isolated sp^2 carbon pairs, they lack effective intercell-interaction, resulting in much less dispersed states in pentadiamond. We have also considered the effect of a mechanical strain on the electronic band gap of pentadiamond, by applying isotropic compression and expansion from -4% up to +4% [44]. We find that the general features of the band structure, including band gap transition k-points and band edge dispersions, remain invariant with strain. However, as shown in Fig. S1 of the Supplementary Information, the band gap increases almost linearly from 3.41 eV at -4% compression to 3.78 eV at a 4% expansion. This is the opposite of what we have previously found in two-dimensional carbon-based materials [45].

We also investigate the optical properties of pentadiamond and compare it with diamond. To this aim we calculate frequency-dependent absorption coefficients using the HSE06 functional, as shown in Fig. 4. Due to their symmetry, the absorption spectra of each allotrope is independent of the polarization of light along the [100], [010], and [001] crystallographic orientations. For pentadiamond the first absorption peak appears at 4.25 eV which is in the ultraviolet energy range and it is due to π(C-C)-π^*(C-C) transitions. Meanwhile, the first absorption peak for diamond occurs at 7 eV, with the remaining absorption peaks farther into the UV region. Pentadiamond exhibits a remarkable absorption coefficient (10^5 cm^{-1}) in the middle UV region of the spectrum, as expected from its much smaller band gap (3.58 eV) relative to diamond (5.27 eV). Nonetheless, it should be noted that the absorption edge cor-

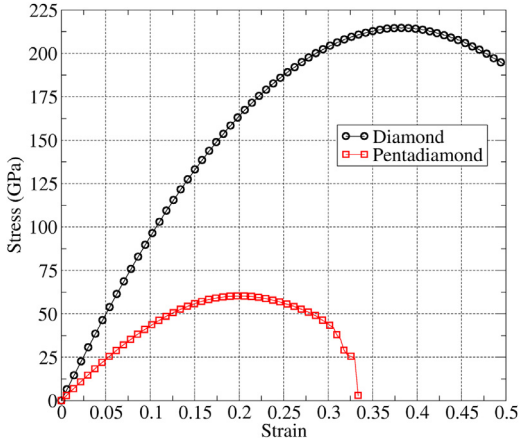

Fig. 5. Uniaxial stress-strain response of pentadiamond and diamond. The tensile strength of pentadiamond in 60.3 GPa, much smaller than 215 GPa for diamond.

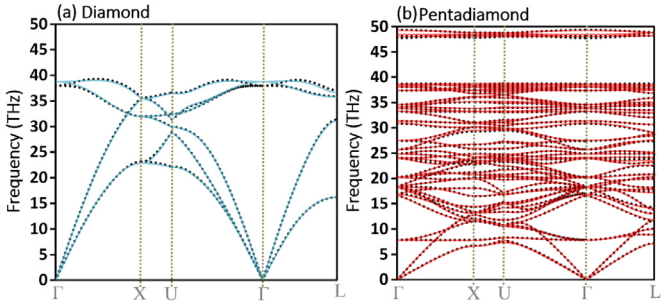

Fig. 6. Phonon dispersion relations of (a) diamond and (b) pentadiamond obtained with the DFPT method (black circles) and state-of-the-art machine-trained MTPs (continuous lines).

responding to the bulk band gaps of pentadiamond and diamond are suppressed due to their indirect transition nature.

We next examine the mechanical properties of diamond and pentadiamond. It is worth noting that the mechanical properties are evaluated at the ground state and thus temperature effects are not considered. For diamond the elastic constants are $C_{11} = 1058.3$ GPa and $C_{12} = 132.2$ GPa, while for pentadiamond we obtain $C_{11} = 539.5$ GPa and $C_{12} = 108.8$ GPa. Therefore, it is clear that the elastic constants of pentadiamond are smaller than the corresponding ones in diamond. For the elastic moduli, we obtain 1025.3 GPa for diamond and 495.6 GPa for pentadiamond. Once again, diamond appears to remain the toughest bulk carbon allotrope.

We further probe the mechanical properties of pentadiamond by investigating its stress-strain behavior under uniaxial deformation. In this case, after applying the loading strain, the simulation box was relaxed along the other two Cartesian directions to reach a negligible stress after a geometry optimization. According to the results shown in Fig. 5, the tensile strength of pentadiamond is just 60.3 GPa, much smaller than the 215 GPa found for diamond. Furthermore, the ultimate strain of pentadiamond is almost half of the corresponding value for diamond. These results clearly show that, although pentadiamond might present interesting physical properties, its mechanical strength is not comparable to diamond's, as originally claimed in the work of Fujii et al [21].

We now study the phononic properties of pentadiamond and compare it with those of diamond. Phonon frequencies were calculated with the DFPT method and well as machine-trained MTPs, with a remarkable agreement between methods as shown in Fig. 6. Pentadiamond does not present imaginary frequencies, which further corroborates its structural stability. Comparing the phonon dispersion curves for both allotropes, we observe two major differences between them. First, the acoustic modes in diamond show steeper dispersion and reach higher frequencies when compared to the acoustic modes in pentadiamond. Second, pentadiamond presents a large number of optical phonon modes with almost flat dispersion. These observations are consistent with higher phonon scattering in pentadiamond which should lead to a lower thermal conductivity when compared to diamond.

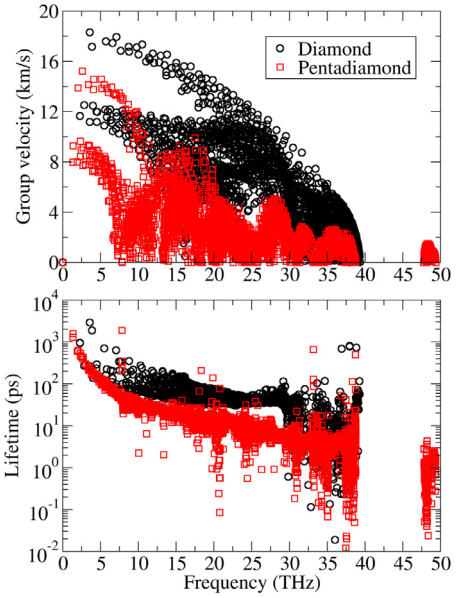

Fig. 7. Phonon group velocities and lifetimes as a function of frequency for diamond and pentadiamond at room temperature.

We have also compared the phonon group velocities and lifetimes of diamond and pentadiamond, as shown in Fig. 7. In the case of diamond, the maximum group velocity for acoustic modes is 17.28 km/s, while for pentadiamond it is 13.14 km/s. Moreover, all acoustic modes in diamond show higher group velocities than the corresponding ones in pentadiamond. As expected, the high-frequency optical modes in pentadiamond present very low group velocities, contributing to larger scattering rates and a lower thermal conductivity. Comparing the phonon lifetimes we find that they are longer in the case of diamond throughout the frequency spectrum.

At last, we present the room temperature thermal conductivity of pentadiamond and compare it with diamond. One important factor in the solution of the Boltzmann equation implemented in ShengBTE is the Brillouin zone sampling density, defined by the number of q-points along each direction. We begin from very coarse grids with 3×3×3 q-points and go up to finer grids of 13×13×13 q-points for pentadiamond and 27×27×27 for diamond. Pentadiamond has a larger number of phonon modes, as seen from the phonon dispersion curves, and the calculation for denser grids become prohibitive. Therefore, in order to estimate the thermal conductivity of pentadiamond in the fully converged limit, we rely on an extrapolation proposed in the original ShengBTE publication [39]. Considering a $N_q \times N_q \times N_q$ grid, the thermal conductivity can be written as $\kappa(N_q) = \kappa[1 - \exp(-N_q/a)]$, where a is a numerical constant and κ is the intrinsic conductivity.

Fig. 8 shows the data points obtained with force constants from the MTP, as well as the extrapolation function. We obtain $\kappa = 2490$ W/m-K for diamond and $\kappa = 427$ W/m-K for pentadiamond, consistent with the diferences in phonon dispersions, group velocities and lifetimes, as discussed above. For comparison, the thermal conductivity of diamond calculated with the Green-Kubo formula in classical molecular dynamics based on the Tersoff potential yields

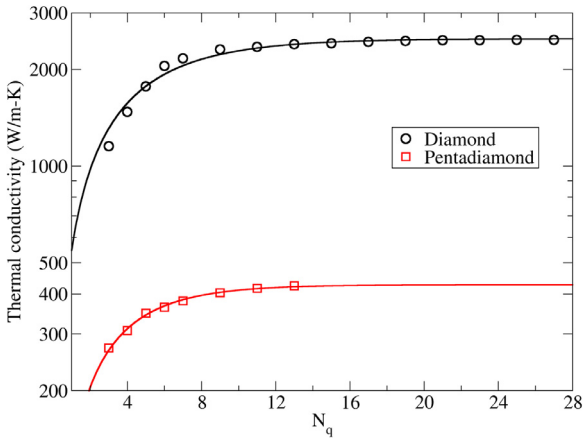

Fig. 8. Room temperature lattice thermal conductivity of diamond and pentadiamond as a function of the number of q-points. The sampling grid is $N_q \times N_q \times N_q$.

a value of 1950 ± 40 W/m-K [46]. The lower value in the latter case is to be expected, since the Green-Kubo method allows for scattering processes involving more than 3 phonons. Finally, we notice that even though the lattice thermal conductivity of pentadiamond is less than one fifth of the corresponding value for diamond it is still among the highest for bulk materials, being comparable to the thermal conductivity of copper.

4. Conclusions

In summary, we performed first-principles calculations to explore the electronic structure, optical characteristics, mechanical response and lattice thermal conductivity of pentadiamond, performing a direct comparison with diamond. Electronic structure calculations based on the hybrid HSE06 functional yield an indirect band gap of 3.58 eV for pentadiamond, well within the wide band gap semiconductor domain. The absorption spectra of diamond and pentadiamond, also calculated with HSE06, reveals pentadiamond's large absorption in the middle UV region, where diamond does not absorb light. The elastic modulus and tensile strength of pentadiamond were found to be 496 GPa and 60 GPa, respectively, considerably lower than the corresponding values for diamond. Finally, solving the Boltzmann transport equation, with anharmonic force constants evaluated via machine-learning interatomic potentials, the thermal conductivity of pentadiamond was found to be 427 W/m-K, which amounts to less than one fifth of that for diamond. Our results highlight that pentadiamond shows appealing features for applications in electronics and optical devices. Moreover, despite exhibiting lower thermal conductivity and mechanical strength than diamond, these properties of pentadiamond are among the highest in comparison with other bulk structures.

Finally, let us not forget that although pentadiamond has not been synthesized yet, it could be produced via standard copolymerization of hydrocarbon molecules containing pentagonal rings. Once pentadiamond samples are obtained, many of the experimental techniques employed to measure phonon properties in diamond would be readily available. For example, neutron scattering could be used to obtain the phonon dispersion relations in Fig. 6. Furthermore, techniques such as thermal conductivity spectroscopy [47,48] could be employed to directly compare the mean free path of phonons in diamond and pentadiamond, which are directly related to the group velocities and lifetimes presented in Fig. 7. We expect that our results will serve as motivation to experimentalists interested in electronic, optical, mechanical and thermal transport properties of novel carbon allotropes.

Acknowledgements

BM and XZ appreciate the funding by the Deutsche Forschungsgemeinschaft (DFG, German Research Foundation) under Germany Excellence Strategy within the Cluster of Excellence PhoenixD (EXC 2122, Project ID 390833453). BM and XZ are also greatly thankful to the VEGAS cluster at Bauhaus University of Weimar for providing the computational resources. FS thanks the Persian Gulf University Research Council for support of this study. LFCP acknowledges financial support from Conselho Nacional de Desenvolvimento Científico e Tecnológico (CNPq, Grants 309961/2017, 436859/2018 and 313462/2020).

Supplementary material

Supplementary material associated with this article can be found, in the online version, at 10.1016/j.cartre.2021.100036.

References

[1] H.W. Kroto, J.R. Heath, S.C. O'Brien, R.F. Curl, R.E. Smalley, C60: Buckminsterfullerene, Nature 318 (1985) 162.
[2] S. Iijima, Helical microtubules of graphitic carbon, Nature 354 (1991) 56–58. http://www.nature.com/physics/looking-back/iijima/.
[3] K.S. Novoselov, A.K. Geim, S.V. Morozov, D. Jiang, Y. Zhang, S.V. Dubonos, I.V. Grigorieva, A.A. Firsov, Electric field effect in atomically thin carbon films., Science (80-.) 306 (2004) 666, doi:10.1126/science.1102896. http://www.ncbi.nlm.nih.gov/pubmed/15499015.
[4] A.K. Geim, K.S. Novoselov, The rise of graphene., Nat. Mater. 6 (3) (2007) 183, doi:10.1038/nmat1849. http://www.ncbi.nlm.nih.gov/pubmed/17330084.
[5] A.H. Castro Neto, F. Guinea, N.M.R. Peres, K.S. Novoselov, A.K. Geim, The electronic properties of graphene, Rev. Mod. Phys. 81 (1) (2009) 109–162, doi:10.1103/RevModPhys.81.109.
[6] J.N. Coleman, U. Khan, W.J. Blau, Y.K. Gun'ko, Small but strong: A review of the mechanical properties of carbon nanotubepolymer composites, Carbon N. Y. 44 (9) (2006) 1624–1652, doi:10.1016/j.carbon.2006.02.038. http://linkinghub.elsevier.com/retrieve/pii/S0008622306001229.
[7] Z.H. Ni, T. Yu, Y.H. Lu, Y.Y. Wang, Y.P. Feng, Z.X. Shen, Uniaxial strain on graphene: Raman spectroscopy study and band-gap opening., ACS Nano 2 (11) (2008) 2301–2305, doi:10.1021/nn800459e. http://www.ncbi.nlm.nih.gov/pubmed/19206396.
[8] S. Berber, Y.K. Kwon, D. Tománek, Unusually High Thermal Conductivity of Carbon Nanotubes, Phys. Rev. Lett. 84 (20) (2000) 4613–4616, doi:10.1103/PhysRevLett.84.4613.
[9] L.F.C. Pereira, I. Savić, D. Donadio, Thermal conductivity of one-, two- and three-dimensional sp 2 carbon, New J. Phys. 15 (10) (2013) 105019, doi:10.1088/1367-2630/15/10/105019. http://stacks.iop.org/1367-2630/15/i=10/a=105019?key=crossref.d97b982766d22ef14fd0a5354c3439fe.
[10] X. Xu, L.F.C. Pereira, Y. Wang, J. Wu, K. Zhang, X. Zhao, S. Bae, C. Tinh Bui, R. Xie, J.T.L. Thong, B.H. Hong, K.P. Loh, D. Donadio, B. Li, B. Özyilmaz, Length-dependent thermal conductivity in suspended single-layer graphene, Nat. Commun. 5 (2014) 3689, doi:10.1038/ncomms4689.
[11] R.H. Baughman, H. Eckhardt, M. Kertesz, Structureproperty predictions for new planar forms of carbon: Layered phases containing s p 2 and s p atoms, J. Chem. Phys. 87 (11) (1987) 6687–6699, doi:10.1063/1.453405.
[12] G. Li, Y. Li, H. Liu, Y. Guo, Y. Li, D. Zhu, Architecture of graphdiyne nanoscale films, Chem. Commun. 46 (19) (2010) 3256, doi:10.1039/b922733d. http://xlink.rsc.org/?DOI=b922733d.
[13] R. Matsuoka, R. Sakamoto, K. Hoshiko, S. Sasaki, H. Masunaga, K. Nagashio, H. Nishihara, Crystalline Graphdiyne Nanosheets Produced at a Gas/Liquid or Liquid/Liquid Interface, J. Am. Chem. Soc. 139 (8) (2017) 3145–3152, doi:10.1021/jacs.6b12776.
[14] B. Mortazavi, M. Shahrokhi, T. Rabczuk, L.F.C. Pereira, Electronic, optical and thermal properties of highly stretchable 2D carbon Ene-yne graphyne, Carbon N. Y. 123 (2017) 344, doi:10.1016/j.carbon.2017.07.066. http://linkinghub.elsevier.com/retrieve/pii/S0008622317307480.
[15] B. Ram, H. Mizuseki, Tetrahexcarbon: A two-dimensional allotrope of carbon, Carbon N. Y. 137 (2018) 266–273, doi:10.1016/j.carbon.2018.05.034. https://linkinghub.elsevier.com/retrieve/pii/S0008622318304937.
[16] M.L. Álvares Paz, A. Saraiva-Souza, V. Meunier, E.C. Girão, Naphthylenes: 1D and 2D carbon allotropes based on naphthyl units, Carbon N. Y. 153 (2019) 792–803, doi:10.1016/j.carbon.2019.07.037. https://linkinghub.elsevier.com/retrieve/pii/S0008622319307249.
[17] L.C. Felix, V. Gaál, C.F. Woellner, V. Rodrigues, D.S. Galvao, Mechanical Properties of Diamond Schwarzites: From Atomistic Models to 3D-Printed Structures, MRS Adv. 5 (33-34) (2020) 1775–1781, doi:10.1557/adv.2020.175. https://www.cambridge.org/core/product/identifier/S2059852120001759/type/journal_article.
[18] F.M. de Vasconcelos, A.G. Souza Filho, V. Meunier, E.C. Girão, Electronic and structural properties of tetragraphenes, Carbon N. Y. 167 (2020) 403–

413, doi:10.1016/j.carbon.2020.05.030. https://linkinghub.elsevier.com/retrieve/pii/S0008622320304711.
[19] L.C. Felix, R.M. Tromer, P.A.S. Autreto, L.A. Ribeiro Junior, D.S. Galvao, On the Mechanical Properties and Thermal Stability of a Recently Synthesized Monolayer Amorphous Carbon, J. Phys. Chem. C 124 (27) (2020) 14855–14860, doi:10.1021/acs.jpcc.0c02999.
[20] J. De Sousa, A. Aguiar, E. Girão, A.F. Fonseca, A. Souza Filho, D. Galvão, Computational study of elastic, structural stability and dynamics properties of pentagraphene membrane, Chem. Phys. 542 (2021) 111052, doi:10.1016/j.chemphys.2020.111052. https://linkinghub.elsevier.com/retrieve/pii/S0301010420311770.
[21] Y. Fujii, M. Maruyama, N.T. Cuong, S. Okada, Pentadiamond: A Hard Carbon Allotrope of a Pentagonal Network of <math display="inline"> <mrow> <msup> <mrow> <mi>sp</mi> </mrow> <mrow> <mn>2</mn> </mrow> </msup> </mrow> </math> and <math display="inline"> <mrow> <msup> <mrow> <mi>sp</mi> </mrow> <mrow>, Phys. Rev. Lett. 125 (1) (2020) 016001, doi:10.1103/PhysRevLett.125.016001.
[22] Y. Fujii, M. Maruyama, N.T. Cuong, S. Okada, Retraction: Pentadiamond: A Hard Carbon Allotrope of a Pentagonal Network of <math display="inline"> <mi>s</mi> <msup> <mi>p</mi> <mn>2</mn> </msup> </math> and <math display="inline"> <mi>s</mi> <msup> <mi>p</mi> <mn>3</mn> </msup> </math> C Atoms [Phys., Phys. Rev. Lett. 125 (7) (2020) 079901, doi:10.1103/PhysRevLett.125.079901.
[23] G. Kresse, J. Furthmüller, Efficient iterative schemes for ab initio total-energy calculations using a plane-wave basis set, Phys. Rev. B 54 (16) (1996) 11169, doi:10.1103/PhysRevB.54.11169.
[24] G. Kresse, J. Furthmüller, Efficiency of ab-initio total energy calculations for metals and semiconductors using a plane-wave basis set, Comp. Mater. Sci. 6 (1) (1996) 15–50, doi:10.1016/0927-0256(96)00008-0. http://linkinghub.elsevier.com/retrieve/pii/0927025696000080.
[25] G. Kresse, D. Joubert, From ultrasoft pseudopotentials to the projector augmented-wave method, Phys. Rev. B 59 (3) (1999) 1758, doi:10.1103/PhysRevB.59.1758.
[26] J.P. Perdew, A. Ruzsinszky, G.I. Csonka, O.A. Vydrov, G.E. Scuseria, L.A. Constantin, X. Zhou, K. Burke, Restoring the Density-Gradient Expansion for Exchange in Solids and Surfaces, Phys. Rev. Lett. 100 (13) (2008) 136406, doi:10.1103/PhysRevLett.100.136406.
[27] G.I. Csonka, J.P. Perdew, A. Ruzsinszky, P.H.T. Philipsen, S. Lebègue, J. Paier, O.A. Vydrov, J.G. Ángyán, Assessing the performance of recent density functionals for bulk solids, Phys. Rev. B 79 (15) (2009) 155107, doi:10.1103/PhysRevB.79.155107.
[28] H.J. Monkhorst, J.D. Pack, Special points for Brillouin-zone integrations, Phys. Rev. B 13 (12) (1976) 5188, doi:10.1103/PhysRevB.13.5188.
[29] J. Heyd, G.E. Scuseria, M. Ernzerhof, Hybrid functionals based on a screened Coulomb potential, J. Chem. Phys. 118 (18) (2003) 8207–8215, doi:10.1063/1.1564060.
[30] A.V. Krukau, O.A. Vydrov, A.F. Izmaylov, G.E. Scuseria, Influence of the exchange screening parameter on the performance of screened hybrid functionals, J. Chem. Phys. 125 (22) (2006) 224106, doi:10.1063/1.2404663.
[31] M. Gajdoš, K. Hummer, G. Kresse, J. Furthmüller, F. Bechstedt, Linear optical properties in the projector-augmented wave methodology, Phys. Rev. B 73 (4) (2006) 045112, doi:10.1103/PhysRevB.73.045112.
[32] A. Togo, I. Tanaka, First principles phonon calculations in materials science, Scr. Mater. 108 (2015) 1–5, doi:10.1016/j.scriptamat.2015.07.021. https://linkinghub.elsevier.com/retrieve/pii/S1359646215003127.
[33] A.V. Shapeev, Moment Tensor Potentials: A Class of Systematically Improvable Interatomic Potentials, Multiscale Model. Simul. 14 (3) (2016) 1153–1173, doi:10.1137/15M1054183.
[34] K.T. Schütt, P.-J. Kindermans, H.E. Sauceda, S. Chmiela, A. Tkatchenko, K.-R. Müller, SchNet: A continuous-filter convolutional neural network for modeling quantum interactions, Adv. Neural Inf. Process. Syst. 30 (2017) 992–1002. http://arxiv.org/abs/1706.08566.
[35] V. Botu, R. Batra, J. Chapman, R. Ramprasad, Machine Learning Force Fields: Construction, Validation, and Outlook, J. Phys. Chem. C 121 (1) (2017) 511–522, doi:10.1021/acs.jpcc.6b10908.
[36] Y. Zuo, C. Chen, X. Li, Z. Deng, Y. Chen, J. Behler, G. Csányi, A.V. Shapeev, A.P. Thompson, M.A. Wood, S.P. Ong, Performance and Cost Assessment of Machine Learning Interatomic Potentials, J. Phys. Chem. A 124 (4) (2020) 731–745, doi:10.1021/acs.jpca.9b08723.
[37] B. Mortazavi, I.S. Novikov, E.V. Podryabinkin, S. Roche, T. Rabczuk, A.V. Shapeev, X. Zhuang, Exploring phononic properties of two-dimensional materials using machine learning interatomic potentials, Appl. Mater. Today 20 (2020) 100685, doi:10.1016/j.apmt.2020.100685. https://linkinghub.elsevier.com/retrieve/pii/S2352940720301323.
[38] B. Mortazavi, E.V. Podryabinkin, I.S. Novikov, T. Rabczuk, X. Zhuang, A.V. Shapeev, Accelerating first-principles estimation of thermal conductivity by machine-learning interatomic potentials: A MTP/ShengBTE solution, Comput. Phys. Commun. 258 (2021) 107583, doi:10.1016/j.cpc.2020.107583. https://linkinghub.elsevier.com/retrieve/pii/S0010465520302800.
[39] W. Li, J. Carrete, N.A. Katcho, N. Mingo, ShengBTE: A solver of the Boltzmann transport equation for phonons, Comp. Phys. Comm. 185 (6) (2014) 1747–1758, doi:10.1016/j.cpc.2014.02.015. http://linkinghub.elsevier.com/retrieve/pii/S0010465514000484.
[40] Z. Li, Y. Wu, S. Zhang, Y. Zhang, Y. Gao, K. Luo, Z. Zhao, J. He, Pentadiamond-like Metallic Hard Carbon Nitride, J. Phys. Chem. C 124 (45) (2020) 24978–24983, doi:10.1021/acs.jpcc.0c07648.
[41] R.M. Tromer, L.C. Felix, C.F. Woellner, D.S. Galvao, A DFT investigation of the electronic, optical, and thermoelectric properties of pentadiamond, Chem. Phys. Lett. 763 (2021) 138210, doi:10.1016/j.cplett.2020.138210. https://linkinghub.elsevier.com/retrieve/pii/S0009261420311143.
[42] R. Kalish, Diamond as a unique high-tech electronic material: difficulties and prospects, J. Phys. D. Appl. Phys. 40 (20) (2007) 6467–6478, doi:10.1088/0022-3727/40/20/S22.
[43] C.J. Wort, R.S. Balmer, Diamond as an electronic material, Mater. Today 11 (1-2) (2008) 22–28, doi:10.1016/S1369-7021(07)70349-8. https://linkinghub.elsevier.com/retrieve/pii/S1369702107703498.
[44] M. Tabatabaeichehr, H. Mortazavi, The effectiveness of aromatherapy in the management of labor pain and anxiety, Ethiopian Journal of Health Sciences 30 (2020) 449–458, doi:10.4314/ejhs.v30i3.16.
[45] B. Mortazavi, O. Rahaman, T. Rabczuk, L.F.C. Pereira, Thermal conductivity and mechanical properties of nitrogenated holey graphene, Carbon N. Y. 106 (2016) 1, doi:10.1016/j.carbon.2016.05.009. http://linkinghub.elsevier.com/retrieve/pii/S0008622316303591.
[46] Z. Fan, L.F.C. Pereira, H.-Q. Wang, J.-C. Zheng, D. Donadio, A. Harju, Force and heat current formulas for many-body potentials in molecular dynamics simulations with applications to thermal conductivity calculations, Phys. Rev. B 92 (9) (2015) 094301, doi:10.1103/PhysRevB.92.094301.
[47] A.J. Minnich, J.A. Johnson, A.J. Schmidt, K. Esfarjani, M.S. Dresselhaus, K.A. Nelson, G. Chen, Thermal Conductivity Spectroscopy Technique to Measure Phonon Mean Free Paths, Phys. Rev. Lett. 107 (9) (2011) 095901, doi:10.1103/PhysRevLett.107.095901.
[48] A.J. Minnich, Determining Phonon Mean Free Paths from Observations of Quasiballistic Thermal Transport, Phys. Rev. Lett. 109 (20) (2012) 205901, doi:10.1103/PhysRevLett.109.205901.